System Stability Issues Involving Distributed Sources under Adverse Network Conditions

Theodoros Souxes and Costas Vournas
School of Electrical and Computer Engineering
National Technical University of Athens
Athens, Greece
vournas@power.ece.ntua.gr

***Abstract*—This paper focuses on short-term power system instability arising under adverse network conditions and involving Inverter-Based Generation (IBG). This type of instability has not so far been described in power system stability classifications. A simple radial system with IBG is initially examined, in order to classify the possible mechanisms of short-term instability involving converter voltage and current controls. Next, a typical feeder connecting a wind farm taken from the Hellenic Interconnected System is simulated as a case study. Finally, a protection scheme, able to identify and prevent the IBG instability is proposed and simulated to prove its efficiency.**

Keywords—Power System Stability, Inverter-Based Generation, Maximum Power Transfer, Voltage Source Converter.

I. INTRODUCTION

In recent years, although synchronous generators are still dominant in electric power networks, there is an increasing number of inverter-based generators (IBGs) that continuously replace synchronous ones [1]. This evolutionary trend is mainly attributed to the use in Renewable Energy Sources (mostly wind power and photovoltaic panels), but is also related to converter control flexibility, allowing current control, active and reactive power control, as well as voltage control [2], [3].

Various works on converter stability have been reported in recent literature [4], especially focusing on the impact of phase-locked loop (PLL) parameters on the dynamic and steady-state converter behavior [5], [6].

In this paper the focus is not on the internal converter control loop stability, but rather on power system stability issues (especially under adverse network conditions) affecting and influenced by inverter connected generators and their external loop power, voltage, or current controls. In particular the instability investigated is related to the maximum power that can be transferred by the IBG under certain control conditions. It is possible that the instability mechanisms investigated in this paper may eventually result in some form of PLL instability [7], [8], but the instability analyzed here is related to the weakening of the network and is not due to the parameters or the tuning of the PLL.

The paper is structured as follows: in Section II a radial system with IBG connected to a Thevenin equivalent is examined and its external control loops are briefly discussed. Stability issues concerning Voltage Source (VSC) and also Current Source (CSC) Converters are highlighted, with emphasis to the instability occurring under constant voltage or current operation and adverse network conditions.

In Sections III and IV, a detailed dedicated medium voltage (MV) feeder, corresponding to an actual wind farm (WF) installation in the area of Peloponnese in the Hellenic Interconnected System is examined, using Quasi-Steady-State (QSS) simulation [9]. This voltage stability test system is analyzed, focusing mainly on the instability mechanism involving the IBG.

Finally, in Section V, a protection scheme, able to detect and prevent this type of instability is proposed. The protection is implemented by determining a specific threshold in the voltage-current sensitivity, which whenever violated results in partial wind power curtailment. The protection system is simulated to verify its performance and dependability.

II. RADIAL SYSTEM WITH IBG (THEVENIN EQUIVALENT)

A. System Description

A two-bus radial test system is shown in the one-line diagram of Fig. 1. Essentially this consists of the Thevenin equivalent seen from the MV bus of the IBG [10], where E_T, θ_T and $\boldsymbol{Z_T}$ are the Thevenin equivalent voltage magnitude, phase angle and impedance respectively, while θ is the IBG bus phase lead angle. Resistance of the Thevenin equivalent is significant and should not be neglected, as it includes MV network resistance, as well as conductance of active loads.

It is noted at this point that even though this section refers to inverter connected generation, the same analysis applies also for loads connected through converters, in which case the active power P_G will become negative ($P_G < 0$).

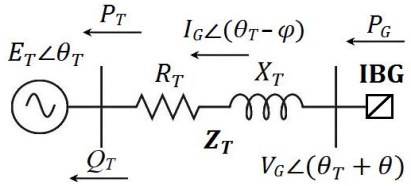

Fig. 1. Thevenin Equivalent of a Radial System seen from the IBG

B. Phase Angle Limits

For the configuration of Fig. 1, the IBG active power generation P_G is expressed as follows, where $\beta=\sin^{-1}(R_T/Z_T)$ is the loss angle of the Thevenin impedance [11]:

$$P_G = \frac{E_T V_G}{Z_T} sin(\theta - \beta) + \frac{V_G^2}{Z_T^2} R_T \quad (1)$$

The maximum IBG active power that can be transferred under constant Thevenin and IBG voltages occurs when the sine becomes 1, i.e. $sin(\theta - \beta) = 1$.

Thus, the maximum generated power limit, when the IBG is controlling its connection point voltage, is similar to an angle stability limit with the only difference being the addition of the transmission loss angle β:

$$\theta_{maxP_G} = \frac{\pi}{2} + \beta \quad (2)$$

The corresponding maximum active generation limit is:

$$P_{Gmax} = \frac{E_T V_G}{Z_T} + \frac{V_G^2}{Z_T^2} R_T \quad (3)$$

Similar to synchronous generator rotor angle stability, if the converter is modifying the voltage V_G phase angle in order to export the generated power, it will reach a stability limit if P_G exceeds (or is equal to) P_{Gmax} defined in (3). As discussed in the introduction, how this instability will affect the converter controls is not of interest here, as it will certainly result in the disconnection of the converter either due to DC capacitor overvoltage or another internal protection.

It should be noted that this phase angle instability risk for converter controlled generators, when network voltages are depressed e.g. due to a fault in the system, is known to the power engineering community and has led to special control schemes, which reduce the generated active power when the voltage at the IBG connection point is below a limit [12], [13].

The effect of resistance on delivered power can be seen considering the active power P_T injected to the Thevenin equivalent voltage source [11], given by:

$$P_T = \frac{E_T V_G}{Z_T} sin(\theta + \beta) - \frac{E_T^2}{Z_T^2} R_T \quad (4)$$

Note that the delivered power is maximized before the stability limit (2) is encountered for a phase angle:

$$\theta_{maxP_T} = \frac{\pi}{2} - \beta \quad (5)$$

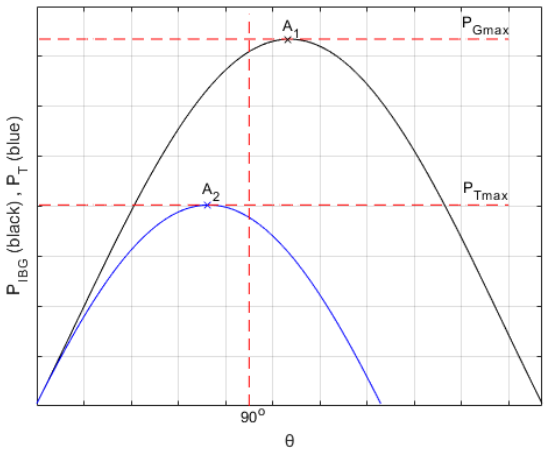

Fig. 2. P_G, P_T curvers as a function of lead angle θ (assuming $\beta \approx 17^o$)

The active power transfers P_G and P_T are shown in Fig. 2, plotted as functions of the IBG bus voltage phase angle θ. Point A_1 denotes the phase angle stability condition (maximum active power for P_G), while point A_2 is where the delivered power P_T is maximized.

As clearly seen in Fig. 2, before meeting the stability limit (2), the exported power to the grid has already passed the maximum point condition (5) and thus the generated power after point (5) is only increasing the losses. Hence, this type of phase angle instability is not expected to be met in resistive networks during normal operation, as it appears for impractical values of phase angle.

C. Stability Limit under Constant Current

Consider now the case where the IBG is initially controlling its terminal voltage under adverse network conditions, for instance while the Thevenin equivalent voltage slowly drops. As maintaining the terminal voltage will require more reactive generation, it is likely that eventually the converter current will reach its rated value. In such cases, the IBG is expected to operate with a constant current equal to its limit.

Under constant current operation, the active power P_T delivered to the Thevenin equivalent of Fig. 1 can be expressed as:

$$P_T = real(\boldsymbol{E_T I_G^\star}) = E_T I_G cos\varphi \quad (6)$$

where φ is the phase angle of converter current with respect to the Thevenin voltage (Fig. 1).

On the other hand, the active power generated by the IBG is also covering the active loses, which, for constant IBG current, are also constant. Thus:

$$P_G = E_T I_G cos\varphi + I_G^2 R_T \quad (7)$$

Hence, under constant current operation, the maximum IBG active power generation limit occurs when the power factor at the Thevenin end becomes unity, i.e. $cos\,\varphi = 1$. Assuming that the current has reached its limit, i.e. $I_G = I^{lim}$, the generated power limit is:

$$P_G^{lim} = I^{lim}(E_T + I^{lim} R_T) \quad (8)$$

In case the generated power exceeds the limit (8) the system will become unstable. This short-term instability will occur regardless of the type of converter control, i.e. whether the converter operates as a current source, or as a voltage source controlling the current. These two cases are investigated separately considering the IBG first as a Current Source Converter and then as a VSC controlling the current to its limit value.

For the CSC case, after the current limiter has been activated, the RMS value of the converter current I_G is held constant at a value equal to I^{lim}. As a result, in order to provide the active power P_G to the grid, the converter controls the current phase φ. However, if the IBG active power is greater than the limit (8) and the system is unable to transfer the injected active power, the phase φ has no solution (no equilibrium condition exists) and consequently the CSC control

becomes unstable. Thus, the converter will be disconnected, as the power not exported will create an overvoltage of the converter DC side capacitor.

If, on the other hand, the VSC scheme is considered, the converter current limiter (when activated) is controlling the converter voltage V_G, in order to keep the current below or equal to I^{lim}.

While the generated active power remains below the limit expressed in (8), i.e. $P_G < P_G^{lim}$, lowering the voltage will result in less reactive power generated and thus in a lower current magnitude. However, if the generated active power becomes greater that the limit, i.e. $P_G > P_G^{lim}$, the voltage can no longer contain the current RMS value, as for either decreasing or increasing the voltage the current will increase and the converter will have to be disconnected by overcurrent protection.

This instability mechanism can be expressed through the converter current-voltage (*I-V*) sensitivity becoming equal to zero:

$$\frac{\partial I_G}{\partial V_G} = 0 \tag{9}$$

As shown in the Appendix, condition (9) is equivalent to condition (8), i.e. to the condition $cos\,\varphi=1$ in (6), (7).

III. Voltage Stability Test System

A. Distribution MV Feeder Model and Controls

The test system simulated in this Section is seen in Fig. 3 and consists of a weak transmission corridor, in the middle of which an Inverter Based WF is connected through a dedicated MV feeder. The transmission corridor is represented by two equal reactances *X* on the source and load side of the WF connection substation. The transmission system is fed by a constant voltage source *E* and the remote load is connected to the load bus at the end of the corridor with a voltage V_L. Load is represented as a conductance *G* with unity power factor (load reactive power is considered fully compensated). A slow load conductance ramp with an increase rate of 0.1% per second is simulated. During the load ramp, all the automatic controls of the feeder, i.e. switched capacitors B_C and Load Tap Changer (LTC) automatic control of voltage V_2 are simulated, as well as the active and reactive injection at the WF connection point as detailed in [10], [14], [15].

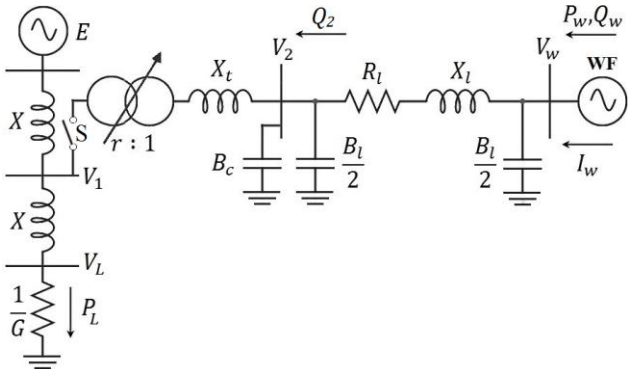

Fig. 3. Complete Test System single-line diagram

The feeder values used correspond to an actual wind farm (WF) installation in the area of Peloponnese in the Hellenic Interconnected System. The test system data are summarized in Table I.

TABLE I. Test System Data

WF Detailed Data (pu on 100MVA)							
Sn (MVA)	***E***	***X***	X_t	R_l	X_l	I^{lim}	V_{thr}
36	0.9778	0.2	0.4	0.015	0.2	0.36	0.90

The initial operating point P_{Wo}, V_{1o}, r_o, corresponding to a summer 2010 snapshot, is seen in Table II. With these data, the system of Fig.3 is initialized for zero load and unity WF power factor, i.e. G_o=0 and Q_{Wo}=0:

TABLE II. Initial Operating Point (pu on 100MVA)

P_{Wo}	V_{1o}	r_o	G_o	Q_{Wo}
0.0176	0.9777	0.9875	0	0

The dynamic representation of feeder controls is presented below. The discrete LTC controller is modelled by the difference equation:

$$r^{(k+1)} = \begin{cases} r^{(k)} + \Delta r, \text{if } V_2 > V_{2,max} \text{ and } r^{(k)} < r_{max} \\ r^{(k)} - \Delta r, \text{if } V_2 < V_{2,min} \text{ and } r^{(k)} > r_{min} \\ r^{(k)} \quad , \quad \text{otherwise} \end{cases} \tag{10}$$

where $r^{(k)} = r(t_k)$ is the transformer ratio at time t_k, r_{min} to r_{max} the tap range boundaries, V_2 the controlled distribution side voltage and $V_{2,min}$ to $V_{2,max}$ its narrow deadband. Tap ratio step Δr is considered constant and one tap change is performed each time V_2 remains outside its deadband for a time delay of T_{LTC}.

The automatic switched capacitor discrete time controller is modelled by the difference equation:

$$B_c^{(k+1)} = \begin{cases} B_c^{(k)} + \Delta B_c, \text{if } V_1 < V_{1,min} \text{ and } B_c^{(k)} < B_{c_{max}} \\ B_c^{(k)} - \Delta B_c, \text{if } V_1 > V_{1,max} \text{ and } B_c^{(k)} > B_{c_{min}} \\ B_c^{(k)} \quad , \quad \text{otherwise} \end{cases} \tag{11}$$

where, similar to the tap ratio, $B_c^{(k)}$ refers to the capacitor susceptance at time instant t_k and $V_{1,min}$ to $V_{1,max}$ is the transmission voltage V_1 deadband (95% and 105% of the nominal transmission value respectively). As seen in Table III, three switchable banks are connected to the HV/MV substation, each with a susceptance ΔB_c. The time delay before a capacitor bank switching T_{Bc} is assumed substantially larger than T_{LTC}, in order to avoid interactions with the LTC control.

In previous work by the authors [10], [14-15], the automatic switched capacitor controller objective was to keep the reactive power Q_2 coming from the distribution feeder within a specified deadband. As a result, the main focus of this control was the support of the distribution system. However, it was noticed that the capacitor banks were not properly exploited with this control, since not all of them where switched before the maximum power conditions on the transmission corridor were encountered. Thus, in this paper, the switched capacitor banks are assumed to support the transmission system by controlling the HV V_1 whenever the voltage limits shown in (11) are exceeded.

The VSC control of the wind farm converter is assumed almost instantaneous (with a time delay of 1ms) and can operate multiple times within the same simulation step.

Two strategies for the IBG discrete reactive control are considered:

a) Unity Power Factor (UPF): the controller maintains a UPF, thus the wind farm voltage V_w changes in each time step to obtain Q_w=0. This is considered the default operating strategy of the WF with the objective to minimize losses in the absence of any other requirement or incentive.

b) Emergency Maximum Reactive Support (EMRS): the controller initially maintains a UPF as in case *a*, until the primary transmission voltage V_1 falls below a specific threshold V_{thr} (90% in the proposed implementation, as seen in Table I) [10], in which case the WF converter modifies the voltage V_w to its maximum permissible value (V_{Wmax}=1.10 pu in this study, as seen in Table III). Hence, when this signal is issued, the WF initiates maximum reactive support to the transmission system. This operating mode requires of course some previous agreement between the TSO and the WF owner to provide this ancillary service.

The EMRS control is subject to the maximum current limitation of the converter (I^{lim}), as already discussed in Section II.C. This is modelled as follows:

If the WF current exceeds the maximum permitted value, the current limiter control algorithm is activated and applied repeatedly, by reducing the converter voltage, until the current satisfies the inequality constraint ($I_w \leq I^{lim}$). Hence:

$$\text{while } I_{w,i} > I^{lim} \text{ then } V_{w,i} = V_{w,i} - \Delta V \tag{12}$$

where i is the iteration counter. Note that (12) is applied multiple times if necessary with negligible time delay.

After the current is brought below its limit I^{lim}, while both EMRS and current limiter controls are activated, the following terminal voltage restoration control is applied

$$\text{while } I_{w,i} < I^{lim} - \varepsilon \text{ and } V_{w,i} < V_{w\,max} \text{ then } V_{w,i} = V_{w,i} + \Delta V \tag{13}$$

where ε a small positive constant taken equal in per unit to the converter voltage step change ΔV. Clearly, in case the current constraint ($I_w \leq I^{lim}$) is once again violated, control (12) is reinstated.

The data of the automatic control mechanisms are summarized in Table III. The maximum permissible current I^{lim} is taken equal to rated assuming unity nominal power factor, i.e. I^{lim}=0.36 pu on 100 MVA for the wind farm of Table I.

TABLE III. DISCRETE CONTROLLER DATA

r_{min}	r_{max}	Δr (%)	LTC steps	ΔB_c (MVAr)	B_c steps	T_{LTC} (s)	T_{Bc} (s)	V_{Wmax} (pu)	ΔV, ε (pu)
0.8	1.1	0.625	48	4	3	10	60	1.1	0.001

B. Simulation with Variable Wind Speed Time-Series

In order to assess the effect of wind variability, a wind velocity time series is considered as input to the wind generators. The sampling frequency of the time series is equal to 1Hz, with a total duration of 5000s. The WF active power time series used as input to the model of Fig. 3 is seen in Fig. 4 in per unit on the WF rating S_n [13].

It should be noted that the WF active power P_w is subject to a variable setpoint P_{set}, with an initial value equal to the WF rating, i.e. $P_{set}^0 = S_n$. Thus:

$$P_w = \begin{cases} P_{set}, & \text{if } P_{inp} > P_{set} \\ P_{inp}, & \text{otherwise} \end{cases} \tag{14}$$

where P_{inp} the input active power time series of Fig. 4.

The test system of Fig. 3 is simulated by constructing the Thevenin equivalent seen from the WF terminals, resulting in the configuration of Fig. 1. This time-varying Thevenin depends on the feeder controls, as well as on load conductance G, which is one of the inputs in every step of the simulation. The other input is the active power P_w of (14), while capacitor susceptance, LTC tap ratio, and WF terminal voltage, are the state variables of the controls defined in (10)-(13).

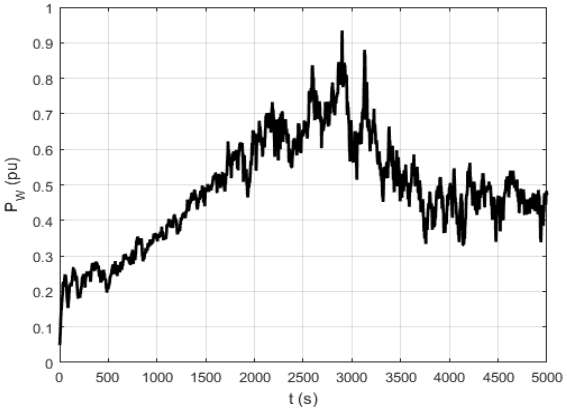

Fig. 4. WF Wind Power Input Time Series (pu on S_n=36 MVA)

The simulation algorithm is the following: for each time step, the operating condition is determined by the above variables (G, r, B_C, V_w, P_w). The voltage phasor angle θ is then directly calculated by solving (1) for $\sin(\theta-\beta)$. After the determination of θ, all other variables are easily evaluated using simple circuit relationships and thus the inputs to all the controllers are determined.

IV. MAXIMUM POWER TRANSFER

The slowly increasing load admittance ramp is simulated with a variable wind power input as discussed above, until the system is past the maximum power transfer (MPT) limit. Thus, the maximum power that can be transferred to the load is indirectly obtained taking into account the effect of the WF and its feeder controls.

In order to compare the increase achieved in the MPT limit due to WF feeder controls, the switch S of Fig. 3 is initially assumed open (base case), therefore, the distribution feeder is not connected to the transmission corridor. As a result, the MPT of the simplified two bus system is according to [9]:

$$P_{L_{max}} = \frac{E^2}{2(2X)} \tag{15}$$

The simulation results are plotted In Fig. 5 in the form of load PV curves, where the load voltage is shown as a function of load consumed power. Separate plots refer to the base case, the UPF control (scheme *a*) and the EMRS control (scheme *b*). In all curves, point C indicates the maximum power transfer to the load bus, point D denotes where the IBG maximum current condition is met, and point E corresponds to the time instant of switching to maximum reactive support. As discussed before, the WF active power input is the one of Fig. 4.

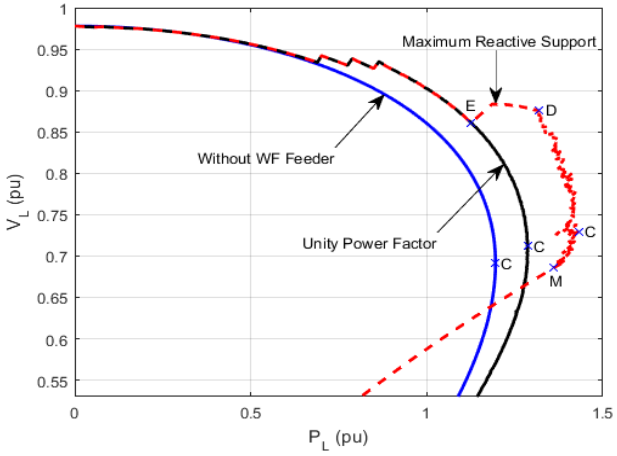

Fig. 5. Load PV without WF Feeder, UPF and EMRS control curves

In Fig. 6 the HV bus voltage V_1 is shown for the EMRS (case *b*) and UPF control (case *a*). The simulation results seen in Figs. 5 and 6 are summarized in Table IV.

TABLE IV. MAXIMUM POWER TRANSFER FROM SIMULATION RESULTS

Variable Wind Power (MW)						
Without WF	***UPF* (*a*)**	***ΔP*$_{Bc}$ *Increase* (*a*)-base case**		***EMRS* (*b*)**	***ΔP*$_{conv}$ *Increase* (*b*)-(*a*)**	
		(MW)	(%)		(MW)	(%)
119.51	128.70	9.19	76.58	143.11	14.41	40.03

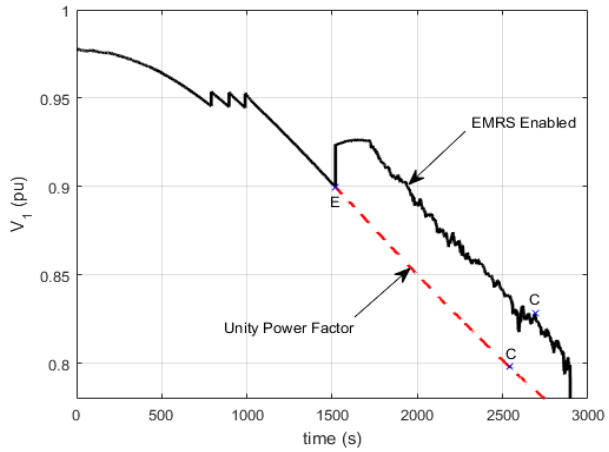

Fig. 6. HV bus controlled transmission voltage V_1

As seen in Fig. 5 and Table IV, a 9.19 MW load margin increase (ΔP_{Bc}) is achieved in case (*a*) with respect to the base case. This increase is mostly due to the automatic capacitors switching, and is roughly 77% of the total capacitor rating (12 MVAr). A further 14.11MW load margin increase (ΔP_{conv}) is achieved in case (*b*) with respect to case (*a*), which is clearly due to the maximum reactive support provided by the WF converter. This increase is roughly 40% of the WF converter MVA rating.

As seen in Fig. 6, the transmission side voltage V_1 falls below the capacitor switching threshold (V_{1min}=0.95pu) at t=730s. Since V_1 remains outside its deadband for a time delay of T_{Bc}, the first capacitor bank switching occurs at t=790s. Following the same procedure, all three capacitor banks have switched on by t=989s. The EMRS control is activated at t=1519s, when the transmission voltage V_1 threshold limit of 90% is reached (point E).

V. STABILITY ANALYSIS

A. IBG Instability

Following the activation of the converter current limiter the instability limit corresponding to the maximum wind power injection is met during the simulation, after the maximum load power transfer limit C is reached (point M in Fig. 5).

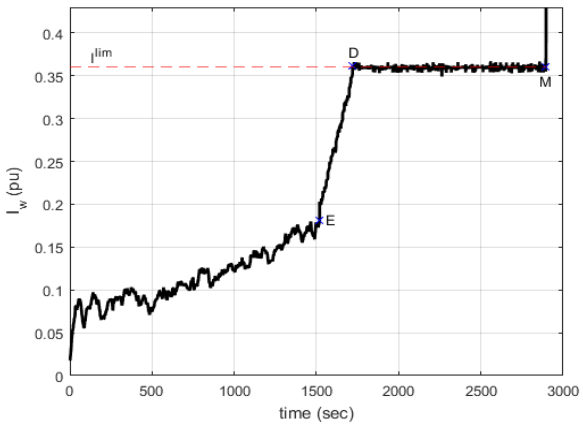

Fig. 7. WF Converter Current with I^{lim}=0.36pu (pu on S_B=100 MVA)

The simulation responses for the examined feeder showing the relevant instability mechanism are plotted in Figures 7 to 10. The VSC model is used (voltage is decreased to contain the converter current within its permissible limit). Point M in the Figures corresponds to the time of converter current control instability. More specifically, the WF converter current I_w is seen in Fig. 7. The maximum current limit is reached at simulation time t=1720s. The current is successfully constrained until the WF active power exceeds the stability limit (8). Thereafter, the system is unable to find a solution to restrict the current and hence the instability occurs at t=2896s. This can be better seen in Fig. 8, where the converter current plot is enlarged.

Figures 9 and 10 are plotted from point D (maximum current reached) to point M (converter control instability). In particular, in Fig. 9 the wind generated power is plotted together with the limits computed using condition (3) and (8).

As seen in Fig. 9, the active power limit varies as the Thevenin equivalent voltage and resistance changes during the load ramp simulation. In the same figure both the phase angle

limit (3) and the constant current stability limit (8) are plotted together with the active generation. As seen, the phase angle stability limit (assuming the converter voltage is held constant at its simulated value) remains well above the rated converter power, while the constant current stability limit is reached at point M.

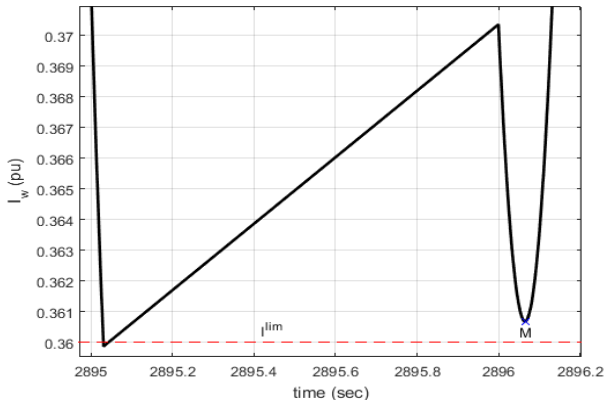

Fig. 8. Enlarged WF Converter Current

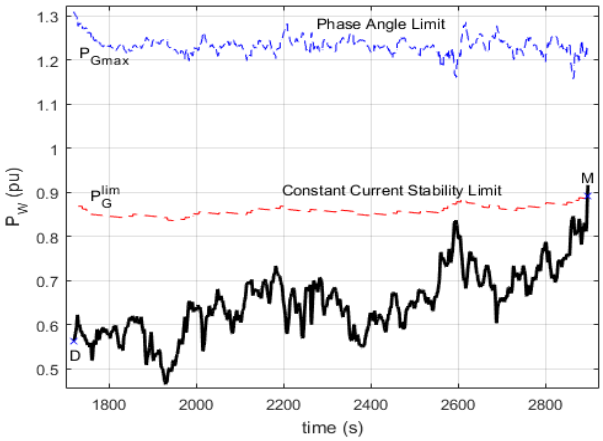

Fig. 9. WF Active Power Generation and limits (pu on S_n=36 MVA)

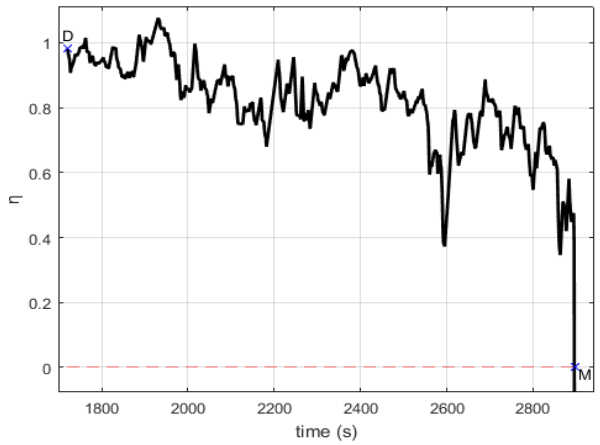

Fig. 10. VSC Current-Voltage Sensitivity (Variable Speed WF)

The loss of current control due to power transfer weakness can also be expressed through current-voltage (*I-V*) sensitivity, described in (9) and seen in Fig. 10.

VI. Instability Detection and Prevention

A. Protection Scheme Against Converter Instability

In this Section, a protection scheme is proposed, which is able to detect and prevent the instability of the converter current limiter. The detection scheme proposed assumes a VSC operation and is applied only when the converter current limitation is active and is reducing the converter voltage, as shown in (12).

The stability monitoring scheme uses inverter current measurements immediately before and after performing a voltage reduction ΔV according to (12). Denoting as $I_{w(i-1)}$ the current before the *i*-th operation of voltage reduction and as I_{wi} the current after voltage reduction, the converter current to voltage sensitivity is directly measured as:

$$\eta_i = \frac{I_{w(i-1)} - I_{wi}}{\Delta V} \tag{16}$$

Note that the sensitivity defined above is positive when the current is decreasing, thus reducing the overcurrent condition. According to stability condition (8) the system is stable while sensitivity is positive (η_i>0). Thus, a stability margin can be maintained by specifying a positive sensitivity threshold η_{min}.

The protection is implemented by curtailing the injected active wind power at the time of sensitivity violation by a preset percentage δ. The time delay for performing the wind curtailment is T_{prot}. If necessary, multiple wind curtailments are made at successive time instants equal to T_{prot}. The parameter values for the protection scheme proposed in this paper are summarized in Table V.

TABLE V. Protection Scheme Data

η_{min}	η_{nom}	δ (%)	T_{prot} (s)
0.6	1.0	10	1

The protection scheme is acting on the wind generation active power setpoint P_{set} of (14) as follows:

$$P_{set}^{(k+1)} = \begin{cases} (1-\delta)P_w^{(k)}, & \text{if } \eta \le \eta_{min} \\ (1+\delta)P_{set}^{(k)}, & \text{if } \eta \ge \eta_{nom} \text{ and } P_{set}^{(k)} < \dfrac{S_n}{(1+\delta)} \\ P_{set}^{(k)}, & \text{otherwise} \end{cases} \tag{17}$$

where P_{set}^0=S_n is the initial active power setpoint, $P_w^{(k)} = P(t_k)$ and $P_{set}^{(k)} = P_{set}(t_k)$ are the active power and power setpoint at time t_k=kT_{prot} respectively, η_{min} and η_{nom} are the threshold and nominal values of the current-voltage sensitivity shown in Table V.

Hence, each time the sensitivity threshold η_{min} is violated, a 10% wind power curtailment occurs, thus settling a new setpoint P_{set}. If and when the nominal sensitivity η_{nom} is restored, a 10% increase in P_{set} is applied at each time instant of the algorithm, until the active power setpoint is restored close to the nominal rating of the converter (S_n).

B. *Protection Scheme Simulation*

The simulation responses of the examined test system of Fig. 3, including the instability detection and prevention scheme, are plotted in Figures 11 to 16. Sequence of events is the same as in Figs. 5-6, up to point N, where the instability is detected by the violation of the sensitivity limit η_{min} and P_{set} is changed accordingly. As seen in Fig. 11, the WF converter current I_w is now successfully constrained throughout the simulation. Figure 12 shows the controlled converter voltage and Fig. 13 the controlled distribution side voltage throughout the simulation. As seen, the approaching instability is detected while the voltage V_w is dropped in order to reduce the reactive generation and consequently the overcurrent. Moreover, while V_2 is successfully constrained within its deadband, the WF voltage drops and stabilizes in constant value of 1.06pu.

The current-voltage sensitivity η plot of Fig. 14 shows that the minimum threshold η_{min} is violated for the first time at t=2560s (Point N). Thus, a curtailment of the wind active power is performed using a setpoint reduction after a time delay T_{prot}, as seen in Fig. 15, where the setpoint changes P_{set} (blue dashed line) and the WF active power generation P_w are plotted. In the same figure the active power stability limit calculated from (8) is plotted with a red dashed line.

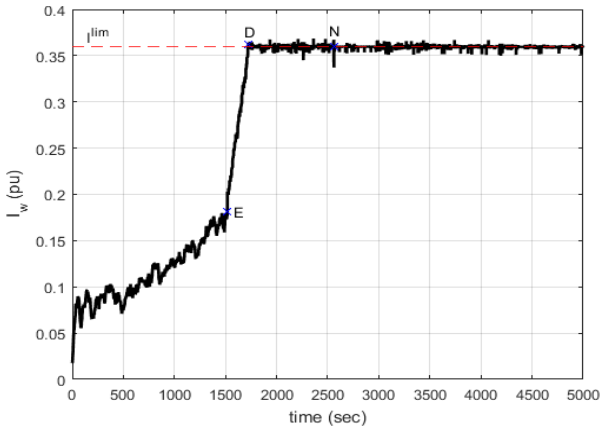

Fig. 11. Constrained WF Converter Current (I^{lim}=0.36pu on S_B=100 MVA)

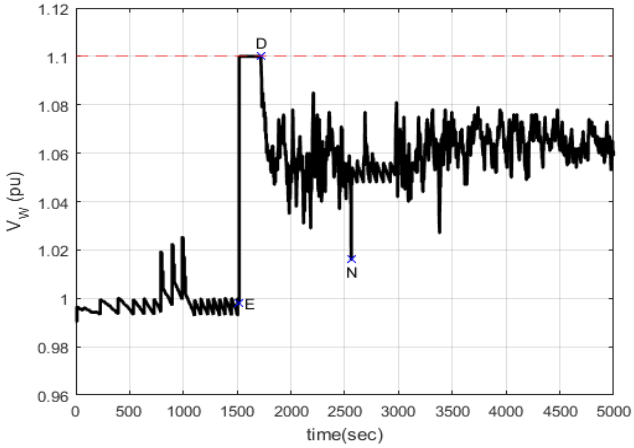

Fig. 12. Controlled Converter Voltage

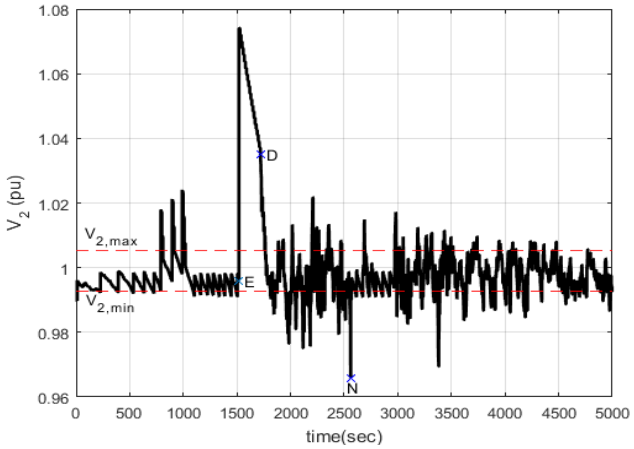

Fig. 13. Controlled Distribution Side Voltage

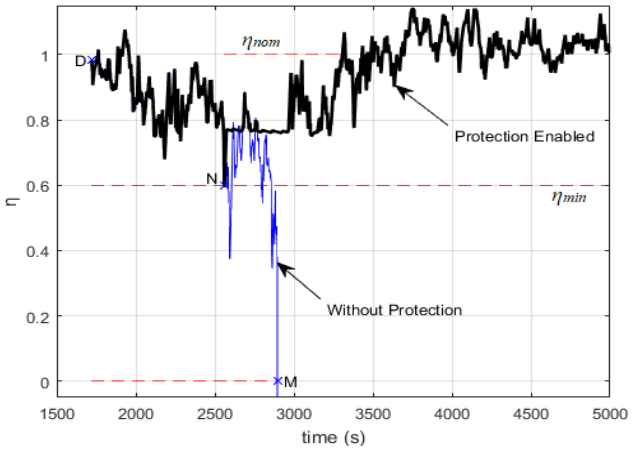

Fig. 14. Current-Voltage Sensitivity with and without Protection scheme

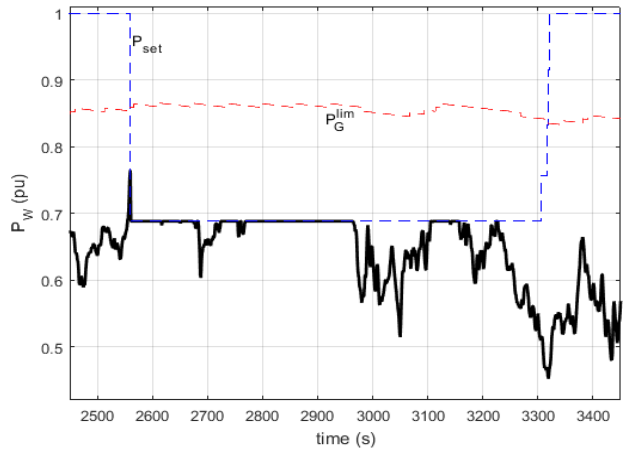

Fig. 15. WF active power generation P_w, limit P_G^{lim} and setpoint P_{set}

As seen in Figs 14 and 15, when the nominal sensitivity η_{nom} is restored after t=3306s, a 10% setpoint increase is successively performed until the active power setpoint approaches again S_n at t=3320s. Finally, the contribution of the protection scheme in the distribution load power-voltage (PV) curve is clearly pointed in Fig. 16.

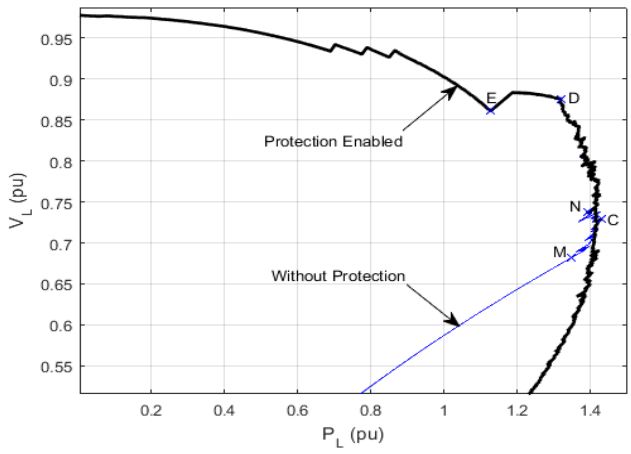

Fig. 16. Load PV curve with and without Protection scheme

VII. Conclusions

In this paper some stability issues associated with generation based on inverters were investigated. In particular, stressed transmission system conditions were examined, in which an IBG was participating in system dynamics by contributing reactive support.

The first part of the paper described two particular types of converter connected generation instability not previously clearly distinguished: maximum power related (i) to voltage phase angle limit and (ii) to current power factor when an overcurrent limitation is encountered.

Angle instability of type (i), which bears a resemblance to synchronous machine rotor angle stability (with the obvious difference of lack of inertia) has been previously reported in the literature, but as shown in Section II of the paper is not very realistic in cases where the inverter based generation is connected in a distribution network where resistances are prominent, because of the stabilization impact of network resistance. Thus, even though in the test system used in this paper line resistance is small, voltage phase instability is not encountered during a voltage stability simulation involving the IBG.

The second type of IBG instability was presented in this paper for the first time and occurs when the converter operates on maximum current. The instability condition for this case was presented in (8) and refers to the inability of the network to receive the generated power (minus active losses) due to its diminishing voltage. This condition is not likely to happen in normal system operation but can occur either during faults (not examined in detail in this paper) or during a voltage instability event.

A case of long-term voltage instability inducing short-term converter instability under maximum current was investigated using a simple test system. The main assumption is that the distributed IBG will contribute to transmission system maximum power transfer by injecting its maximum reactive support using a simple control system based on transmission side voltage threshold.

During such operation, it is essential to note that the converter may have to limit eventually the injected current to its maximum permitted value, thus becoming prone to power factor instability, as was shown in the simulations presented in Section V. It is thus necessary to devise an instability detection and prevention system, so that the IBG can contribute to voltage stability of the transmission system without risking a catastrophic converter instability.

Such a detection and prevention system against converter instability under maximum current was presented and tested in Section VI. It essentially curtails the injected active power when the voltage control mechanism becomes less able to control an overcurrent condition.

As a general comment, this paper investigated converter instability mechanisms when the converter is assigned to support the transmission system through reactive power injection. In the studied cases the converter instability is encountered after the system has reached the long-term voltage stability limit, i.e. after the maximum power transfer denoted by point C in the simulations. This however does not rule out the need to protect the IBG when it is assigned to contribute maximum reactive support to the transmission system.

Appendix: Constant Current Instability Condition

Proposition: The current sensitivity instability condition (9) is equivalent to maximum power condition (8) under constant current, i.e. with the condition cosφ=1 in Fig. 1.

Proof: For the configuration of Fig. 1, where the vector diagram is plotted in Fig. 17, the converter current magnitude I_G can be expressed as:

$$I_G = \frac{|\Delta\hat{V}|}{Z_T} = \frac{\sqrt{V_G^2 + E_T^2 - 2E_T V_G cos\theta}}{Z_T} \quad (18)$$

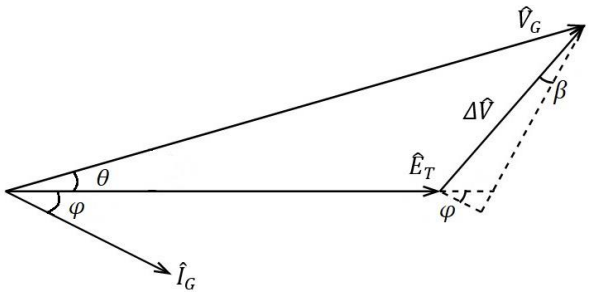

Fig. 17. Vector Diagram of the Radial System (Fig. 1)

From (18) the converter current sensitivity to voltage is calculated as follows:

$$\frac{\partial I_G}{\partial V_G} = \frac{1}{Z_T^2 I_{G_o}} \left(V_{G_o} - E_T \cos\theta_o + \frac{\partial\theta}{\partial V_G} E_T V_{G_o} \sin\theta_o\right) \quad (19)$$

Since the active power generation P_G is considered constant, by differentiating (1) with respect to V_G, the sensitivity of the phase angle θ with respect to V_G can be calculated as follows:

$$0 = \frac{E_T}{Z_T} sin(\theta_o - \beta) + \frac{\partial\theta}{\partial V_G} \frac{E_T V_{G_o}}{Z_T} cos(\theta_o - \beta) + \frac{2V_{G_o} R_T}{Z_T^2}$$

From which:

$$\frac{\partial\theta}{\partial V_G} = \frac{-\frac{sin(\theta_o-\beta)}{V_{G_o}} - \frac{2}{E_T}sin\beta}{cos(\theta_o-\beta)} \tag{20}$$

where $\beta=\sin^{-1}(R_T/Z_T)$ is the loss angle of the Thevenin impedance.

Substituting (20) in (19), the condition of zero current sensitivity ($\partial I_G/\partial V_G = 0$) is:

$$V_{G_o}\,cos(\theta_o-\beta) - E_T cos\theta_o\, cos(\theta_o-\beta) - E_T sin\theta_o\, sin(\theta_o-\beta) - 2V_{G_o} sin\beta sin\theta_o = 0$$

This can be rewritten as:

$$V_{G_o}(cos\theta_o cos\beta + sin\beta sin\theta_o - 2sin\beta sin\theta_o) = E_T cos\beta$$

or:

$$V_{G_o} cos(\theta_o+\beta) = E_T cos\beta = \frac{E_T X_T}{Z_T} \tag{21}$$

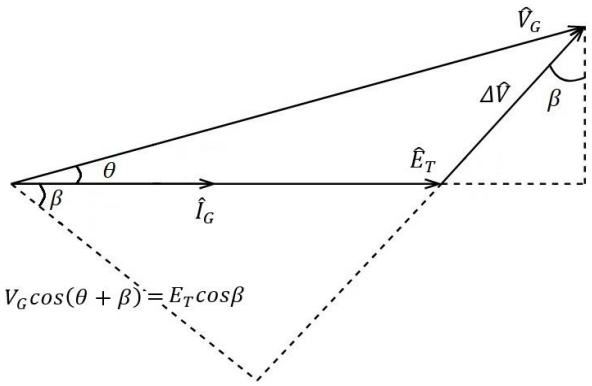

Fig. 18. Vector Diagram with cosφ=1

On the other hand, the reactive power flowing into the Thevenin equivalent voltage source Q_T is given by [11]:

$$Q_T = \frac{E_T V_G}{Z_T} cos(\theta+\beta) - \frac{E_T^2}{Z_T^2} X_T \tag{22}$$

Comparing (21) and (22) it becomes obvious that the condition Q_T =0 (and hence cosφ=1) is equivalent to (9).

q.e.d.

The equivalent of (21) and cosφ=1 is also shown in the vector diagram of Fig. 18, drawn for φ=0º.

REFERENCES

[1] S. Winternheimer, M. Ames and M. Igel, "The challenge to replace synchronous generators by inverter based distributed generation systems," *2015 IEEE 6th International Symposium on Power Electronics for Distributed Generation Systems (PEDG)*, Aachen, 2015, pp. 1-6.

[2] D. Petean, J. C. M. Vieira and R. Q. Machado, "Influence of inverter-based distributed generator interface control on the performance of power distribution systems," *2010 IREP Symposium Bulk Power System Dynamics and Control - VIII (IREP)*, Rio de Janeiro, 2010, pp. 1-8.

[3] H. Shehadeh, V. Boscaino, S. Favuzza and E. R. Sanseverino, "Mathematical modelling of an inverter-based distributed generator," *2016 IEEE 16th International Conference on Environment and Electrical Engineering (EEEIC)*, Florence, 2016, pp. 1-6.

[4] Jia Liu, Y. Miura and T. Ise, "Dynamic characteristics and stability comparisons between virtual synchronous generator and droop control in inverter-based distributed generators," *2014 International Power Electronics Conference (IPEC-Hiroshima 2014 - ECCE ASIA)*, Hiroshima, 2014, pp. 1536-1543.

[5] Ö. Göksu, R. Teodorescu, C. L. Bak, F. Iov and P. C. Kjær, "Instability of Wind Turbine Converters During Current Injection to Low Voltage Grid Faults and PLL Frequency Based Stability Solution," in *IEEE Transactions on Power Systems*, vol. 29, no. 4, pp. 1683-1691, July 2014.

[6] J. Z. Zhou, H. Ding, S. Fan, Y. Zhang and A. M. Gole, "Impact of Short-Circuit Ratio and Phase-Locked-Loop Parameters on the Small-Signal Behavior of a VSC-HVDC Converter," in *IEEE Transactions on Power Delivery*, vol. 29, no. 5, pp. 2287-2296, Oct. 2014.

[7] H. Xin, L. Huang, L. Zhang, Z. Wang and J. Hu, "Synchronous Instability Mechanism of P-f Droop-Controlled Voltage Source Converter Caused by Current Saturation," in *IEEE Transactions on Power Systems*, vol. 31, no. 6, pp. 5206-5207, Nov. 2016.

[8] Shulong Tan, Qing Lv, Hua Geng and Geng Yang, "An equivalent synchronous generator model for current-controlled voltage source converters considering the dynamic of phase-locked-loop," *IECON 2016 - 42nd Annual Conference of the IEEE Industrial Electronics Society*, Florence, 2016, pp. 2235-2240.

[9] T. Van Cutsem, C. Vournas, *Voltage stability of electric power systems*, Kluwer Academic Publishers, 1998, Springer 2008

[10] C. Vournas, I. Anagnostopoulos, T. Souxes, "Transmission support using Wind Farm controls during voltage stability emergencies", Control Engineering Practice, Volume 59, February 2017, Pages 100-110, ISSN 0967-0661

[11] C. Vournas, "Maximum Power Transfer in the Presence of Network Resistance," in *IEEE Transactions on Power Systems*, vol. 30, no. 5, pp. 2826-2827, Sept. 2015.

[12] L.J. Cai, I. Erlich, U. Karaagac, J. Mahseredjian, "Stable operation of doubly-fed induction generator in weak grids", Power & Energy Society General Meeting, 2015.

[13] S. Nanou; G. Tsourakis; C. D. Vournas, "Full-converter wind generator modelling for transient stability studies", IEEE/PES Trondheim Power Tech, June 2011.

[14] C. Vournas and T. Souxes, "Modeling reactive support from distributed resources in hellenic interconnected system," *2016 IEEE Power and Energy Society General Meeting (PESGM)*, Boston, MA, 2016, pp. 1-5.

[15] T. Souxes, G. Tzounas, C. Vournas, "Effect of Wind Variability in the Emergency Reactive Support provided by Wind Farms", *12th IEEE PES PowerTech Conference*, Manchester, June 2017, accepted.